

Optimal navigation of magnetic artificial microswimmers in blood capillaries with deep reinforcement learning

Lucas Amoudruz¹, Sergey Litvinov¹, and Petros Koumoutsakos^{1,*}

¹School of Engineering and Applied Sciences, Harvard University, Cambridge, MA 02138, United States.

*corresponding author: petros@seas.harvard.edu

May 15, 2025

Abstract

Biomedical applications such as targeted drug delivery, microsurgery, and sensing rely on reaching precise areas within the body in a minimally invasive way. Artificial bacterial flagella (ABFs) have emerged as potential tools for this task by navigating through the circulatory system with the help of external magnetic fields. While their swimming characteristics are well understood in simple settings, their controlled navigation through realistic capillary networks remains a significant challenge due to the complexity of blood flow and the high computational cost of detailed simulations. We address this challenge by conducting numerical simulations of ABFs in retinal capillaries, propelled by an external magnetic field. The simulations are based on a validated blood model that predicts the dynamics of individual red blood cells and their hydrodynamic interactions with ABFs. The magnetic field follows a control policy that brings the ABF to a prescribed target. The control policy is learned with an actor-critic, off-policy reinforcement learning algorithm coupled with a reduced-order model of the system. We show that the same policy robustly guides the ABF to a prescribed target in both the reduced-order model and the fine-grained blood simulations. This approach is suitable for designing robust control policies for personalized medicine at moderate computational cost.

1 Introduction

Targeted drug delivery, microsurgery, and microsensing represent important areas of research aimed at revolutionizing precision medicine [1, 2]. These challenging tasks require precise access to target areas in the body, which are often difficult to reach in a non-invasive way. During the past decade, artificial microswimmers have emerged as potent candidates to navigate specific regions of the human body through the circulatory system or tissues [3]. A particular form of artificial microswimmers, known as artificial bacterial flagella (ABFs), features a cork-screw-shaped body propelled by rotating magnetic fields [4]. ABFs have been used in various applications, including navigation through ex-vivo bovine eye tissues [5], assisting spermatozoa in reaching oocytes [6], enhancing nanoparticle transport [7], and carrying drugs for cancer therapy [8].

The swimming properties of ABFs are well understood in the idealized scenario of unbounded, viscous Newtonian fluids [9, 10], near walls [11], and near other swimmers [12]. Venugopalan et al. demonstrated that ABFs can propel in low-concentrated blood suspensions [13]. Alapan et al. have guided microrollers in physiologically relevant blood concentrations with a rotating magnetic field [14]. Qi et al. have conducted numerical simulations of these rollers through blood in straight pipes [15]. However, the swimming characteristics of ABFs within the bloodstream have not been thoroughly investigated. The control of microswimmers for path planning has been the subject of recent advances with the emergence of reinforcement

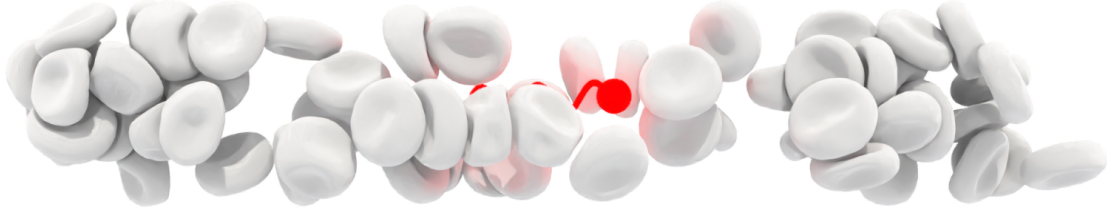


Figure 1: Simulation snapshot of an ABF inside a periodic tube filled with blood. Tube boundaries not shown for visualization purpose.

learning (RL). Muiños-Landin et al. used RL in an experimental setup to control a microswimmer towards a target, without background flow [16]. Similarly, several studies applied RL to guide microswimmers [17] through background flows [18, 19, 20, 21, 22] and perform independent control of multiple ABFs [23, 24] to reach a target or follow a prescribed path [25]. Yang et al. achieved path-planning of point particles between obstacles represented by red blood cells (RBCs) [26]. However, the numerical models used in these studies do not reflect the complex flow patterns present in capillaries, the finite size of the swimmer, and the presence of deformable blood cells, which are known to strongly affect blood flow [27].

In this work, we model and simulate an ABF that evolves in a retinal capillary network. In particular, we learn a control policy that guides the ABF to a prescribed target by imposing an external magnetic field. The geometric representation of the environment is reconstructed from a fundus image of a retinal capillary network [28]. The simulations include an accurate RBC model that was extensively validated on experimental data [29], coupled with the dissipative particle dynamics (DPD) method to resolve the hydrodynamics at the microscale [30]. The control policy is learned with the actor-critic, off policy RL algorithm V-RACER [31]. To substantially reduce the computational cost associated with expensive simulations of the environment, the RL agent is trained on a reduced order model of fine-grained blood simulations. The approach of training the RL agent on a reduced order model has been used in the context of robotics to reduce the number of experiments or expensive simulations [32, 33]. We demonstrate that the policy is robust to noise and transferable to the fine-grained and expensive simulation environment. These results indicate that RL is a promising approach to design control policies with the level of robustness required in biomedical applications. Furthermore, this work demonstrates that ABFs can evolve within the intricate geometry and flow fields of the retinal capillaries to reach precise locations with minimal invasiveness.

2 Artificial microswimmer within blood flow

The simulations consist of an ABF evolving through a network of capillaries filled with blood at a hematocrit $Ht = 25\%$. The ABF has a radius of $2\mu\text{m}$ and a length of $18.37\mu\text{m}$, within the range of the ABFs presented in the literature [9, 10]. Blood is modeled as RBC membranes suspended in plasma and enclosing the cytosol, a fluid 5 times more viscous than plasma [34]. Both plasma and cytosol are viscous Newtonian fluids and are modeled with the DPD method [30]. RBC membranes evolve according to bending forces, and shear forces that are zero when the membrane takes the shape of the stress-free state of the RBC cytoskeleton [35, 36, 29]. An example of simulation of an ABF swimming through a straight tube filled with blood is shown in fig. 1.

The bending energy of the membrane is given by

$$U_{bending} = 2\kappa_b \oint H^2 dA, \quad (1)$$

where the integral is taken over the membrane surface, κ_b is the bending modulus, and H is the local mean curvature. The energy related to the membrane deformation with respect to the stress-free shape (SFS) is

given by

$$U_{in-plane} = \frac{K_\alpha}{2} \oint (\alpha^2 + a_3\alpha^3 + a_4\alpha^4) dA_0 + \mu \oint (\beta + b_1\alpha\beta + b_2\beta^2) dA_0, \quad (2)$$

where the integral is taken over the surface of the SFS, α and β are the local dilation and shear strain invariants of the membrane, respectively, K_α is the dilation elastic modulus, μ is the shear elastic modulus and the coefficients a_3 , a_4 , b_1 and b_2 are parameters that control the non-linearity of the membrane elasticity for large deformations [36].

In addition, the area and volume of the RBC membranes are restricted by penalization energies [37],

$$U_{area} = k_A \frac{(A - A_0)^2}{A_0}, \quad U_{volume} = k_V \frac{(V - V_0)^2}{V_0}, \quad (3)$$

where A_0 and V_0 are the target area and volume of the cell, and A and V are the area and volume of the cell, respectively. Furthermore, k_A and k_V are coefficients that were chosen empirically to enforce small variations of the area and volume over time, within 1%.

Each membrane surface is discretized into a triangle mesh composed of N_v vertices with positions \mathbf{r}_i , velocities \mathbf{v}_i and mass m , $i = 1, 2, \dots, N_v$, evolving through time according to Newton's law of motion. The forces acting on each particle are computed by taking the negative gradient of the discretized energies listed above with respect to particle positions. Finally, the membrane viscosity is modeled through pairwise forces between particles that share an edge,

$$\mathbf{f}_{ij}^{visc} = -\frac{4\eta_m}{\sqrt{3}} (\mathbf{v}_{ij} \cdot \mathbf{e}_{ij}) \mathbf{e}_{ij}, \quad (4)$$

where η_m is the membrane viscosity, $\mathbf{v}_{ij} = \mathbf{v}_i - \mathbf{v}_j$ and \mathbf{e}_{ij} is the unit vector between \mathbf{r}_i and \mathbf{r}_j . Details about the fluid-structure interactions and model parameters are described in ref [38] with extensive validation against experimental data [29].

The ABF is represented as a set of frozen particles and a surface moving as a rigid body. The surrounding solvent particles interact with the ABF particles through DPD forces and are bounced-back from the surface. The magnetic moment \mathbf{m} of the ABF remains constant in the reference frame of the swimmer, perpendicular to its principal axis. The ABF is immersed in an external, uniform magnetic field \mathbf{B} , creating a magnetic torque $\mathbf{T} = \mathbf{m} \times \mathbf{B}$. This torque, combined with the cork-screw shape of the ABF's tail, causes the ABF to propel along its main axis [9]. The external magnetic field varies over time and will be the controlled quantity used to stir the ABF towards its target.

The boundaries of the capillaries were generated from a human retinal vasculature fundus image in Ghassemi et al. [28] (see Supplementary Material). The walls are formed by a layer of frozen DPD particles, of width larger than the interaction cutoff. Furthermore, the DPD particles are bounced-back from the wall surface. The parameters of the DPD forces and interactions between every objects of the simulations are detailed in Amoudruz [38]. To drive the flow, an external body force is applied to the DPD particles, following the approach described in Yazdani et al. [39]. The body force is derived from the pressure gradient obtained by solving the Stokes equation in the same geometry. The flow is solved with *Aphros* [40], assuming a Newtonian fluid, no-slip boundary conditions at the geometry boundaries and a constant velocity at the inlet. In the fine-grained blood simulations, the body forces were scaled to match the Reynolds number at the inlet of the domain. Blood simulations are performed with *Mirheo* [41], a high-performance package for microfluidic simulations on multi-GPU architectures.

Figure 2 shows the swimming speed of a single ABF in a viscous fluid against the rotation frequency of the external magnetic field. The ABF used for this validation case is a helix of diameter 5.294 μm and length 15.75 μm with 3 turns and an ellipsoidal cross section with main diameters 1.192 μm and 2.231 μm . This shape was reproduced to match that of the ABF in experiments from Mhanna et al. [42]. The magnetic

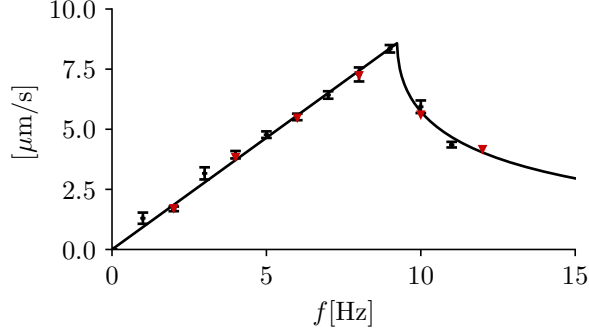


Figure 2: Swimming speed of the ABF against the rotation frequency of the external magnetic field. Triangles are obtained with DPD simulations, crosses are from experiments from Mhanna et al. [42], solid line is a fit to the experimental data with an ODE model [43, 44] (see Supplementary Material).

moment of the swimmer was set to $1 \times 10^{-14} \text{ N m T}^{-1}$, tuned to match the experimental data, and the magnetic field magnitude to 3 mT. Simulations are in good agreement with the experiments by Mhanna et al. [42], validating the DPD method to simulate swimming ABFs in fluids at low Reynolds numbers.

In this work, the ABF has a helical tail and a spherical head, designed to prevent the ABF from getting stuck in RBCs. To increase the swimming speed of the ABF, both the magnetic field frequency and the magnetic moment of the ABF were increased to $f = 1 \text{ kHz}$ and $1 \times 10^{-11} \text{ N m T}^{-1}$, respectively. These adjustments enable the ABF to reach swimming speeds comparable to the inlet flow velocity $U_{in} = 1 \text{ mm s}^{-1}$. Such a high magnetic moment can be achieved by using a magnetic head composed, for example, of nickel, which has a magnetization of $M_{\text{Ni}} = 4.9 \times 10^5 \text{ A m}^{-1}$. For a spherical head of radius $R = 2 \mu\text{m}$, this yields a magnetic moment of $m = M_{\text{Ni}} 4\pi R^3/3 \approx 1.6 \times 10^{-11} \text{ N m T}^{-1}$, demonstrating that the values used in simulations are within experimentally achievable values. Importantly, even at this increased rotation frequency $f = 1 \text{ kHz}$, the Reynolds number remains low, $\text{Re} = R^2 f / \nu \approx 0.004$, justifying the use of the Stokes equation. Therefore, the validation shown in fig. 2 indicates that the DPD method remains appropriate to predict the evolution of ABFs rotating with an angular frequency of $f = 1 \text{ kHz}$.

3 Learning a RL policy with a reduced order model

In this section, we describe the procedure used to learn, with RL, a control policy for guiding the ABF through the retinal capillary network. The goal is to bring the ABF from the network entry point to a specified target location. This is achieved by varying the external magnetic field over time. RL algorithms typically require tens of thousands to millions of episodes to converge. However, each fine-grained simulation of the ABF in the capillary network has a high computational cost of 64 P100 GPUs over 24 hours. Therefore, it is intractable to train the RL agent directly on the high-fidelity model. Instead, the RL agent is coupled with a reduced-order model during training.

The reduced order model represents the ABF as a self-propelling point particle advected by a background velocity field \mathbf{u} . The background velocity field is obtained by solving the Stokes equation within the geometry of the retinal network. The Stokes equation was computed with the grid-based solver *Aphros*. In addition, collisions between the ABF and surrounding RBCs are modeled by a stochastic term, resulting in the stochastic differential equation (SDE)

$$\dot{\mathbf{x}} = \mathbf{u}(\mathbf{x}) + U\mathbf{p} + \sqrt{D}\boldsymbol{\xi}, \quad (5)$$

where \mathbf{p} and U are the direction and magnitude of the ABF self-propelling velocity, respectively. D is a diffusion coefficient and $\boldsymbol{\xi}$ is a Gaussian white noise vector. In addition, the particle bounces back from

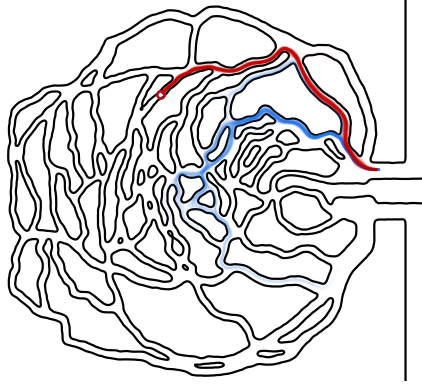


Figure 3: Trajectories of passive tracers (blue) and controlled swimmers (red) obtained from 100 random seeds, with the reduced order model and $D = D_{\text{sim}}$. The circle represents the target. The inlet and outlet have a diameter of $20 \mu\text{m}$.

the wall boundaries. The parameters D and U were calibrated from high-fidelity blood flow simulations of a single ABF in a straight pipe of radius typically found in capillaries (see Supplementary Material). We neglect the rotation dynamics of the ABF, as the reorientation time scale $1/f = 10^{-3} \text{ s}$ is 20 times faster than the typical time scale associated with flow velocity gradients, $2R_{\text{in}}/U_{\text{in}} = 2 \times 10^{-2} \text{ s}$.

The system is advanced in time with a piecewise constant action \mathbf{p} , updated every Δt units of time. The direction \mathbf{p} is computed from the ABF’s position \mathbf{x} through the control policy, $\mathbf{p} = \hat{\mathbf{p}}/|\hat{\mathbf{p}}|$, $\hat{\mathbf{p}} = \pi(\mathbf{x})$. Each episode ends if the simulation time exceeds a maximum time T_{max} or if the ABF reaches the target within a distance δ . The initial position of the ABF at the beginning of each episode is sampled from a set of positions that are along the downstream vessels of the target (see Supplementary Material). The reward at step t is expressed as

$$r_t = -C\Delta t + \|\mathbf{x}_{t-1} - \mathbf{x}_{\text{target}}\| - \|\mathbf{x}_t - \mathbf{x}_{\text{target}}\|, \quad (6)$$

where $C > 0$ is a constant and $\mathbf{x}_{\text{target}}$ is the target position. The first term in eq. (6) penalizes long trajectories, while the second term is a reward shaping that is positive when the ABF progresses towards its target [45].

We train the policy using V-RACER [31], an actor-critic off-policy RL algorithm that was applied to falling objects [46], magnetic microswimmers [23] and self-propelling fish [47, 48]. The algorithm is implemented in *Korali* [49]. Each episode consists of about 500 experiences, and we train the agent over 10 000 episodes.

To test the policy, we generate 100 trajectories with eq. (5), both with the trained policy and for passive tracers ($U = 0$). These trajectories are shown in fig. 3. Passive tracers are much more sensitive to noise than controlled swimmers, and their trajectories end at various locations in the geometry. Passive tracers do not reach the target, as opposed to swimmers that follow the RL policy.

The robustness of the control policy is assessed by varying the magnitude of noise D and measuring the success rate, defined as the number of times the particle reaches the target out of 1000 trials divided by the number of trials. Figure 4 demonstrates that the control policy brings the swimmer to its target more than 98% of the time when $D < 10D_{\text{sim}}$, and 100% of the time when the noise is comparable to that measured from the fine-grained simulations, D_{sim} . Increasing the noise level further results in lower success rates. However, the success rate remains above 85% when $D \leq 20D_{\text{sim}}$. In comparison, passive tracers never reached the target for any values $D \in [0, 20D_{\text{sim}}]$ in our experiments.

Figure 5 shows the policy at bifurcations. The streamlines of the directions obtained from the policy, $\mathbf{p} = \hat{\mathbf{p}}/|\hat{\mathbf{p}}|$, $\hat{\mathbf{p}} = \pi(\mathbf{x})$, converge to a line that connects the starting point to the target. This line seems to

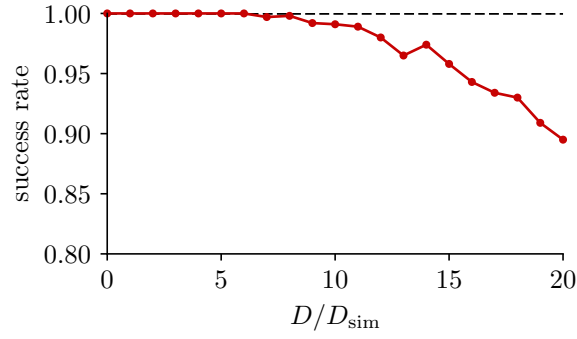


Figure 4: Success rate of the control policy against the noise level D relative to that measured from the fine-grained simulations D_{sim} .

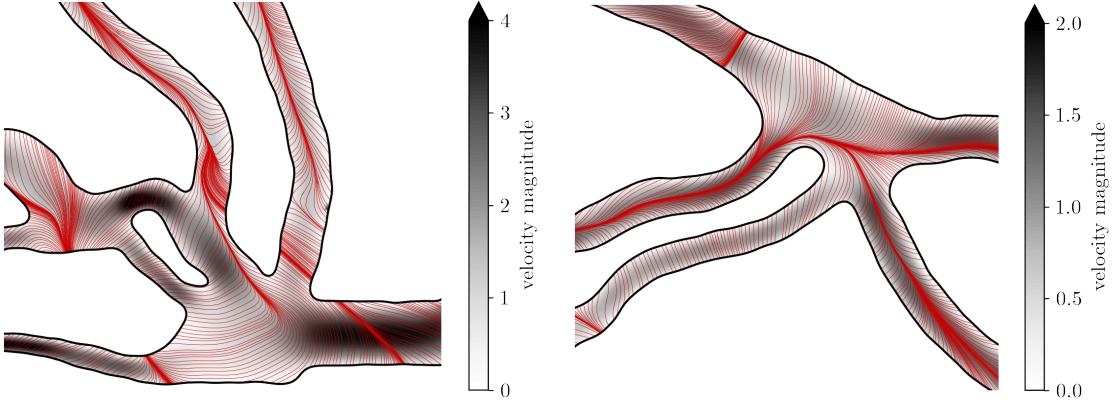


Figure 5: Streamlines of the policy at two bifurcations along the optimal path. The direction chosen by the agent is parallel to the streamlines. The background colors indicate the background velocity magnitude.

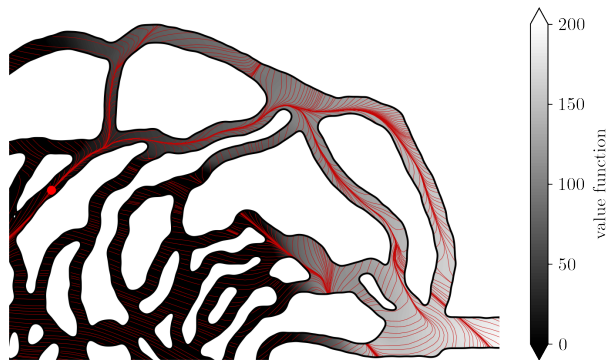


Figure 6: Streamlines of the policy within the capillaries (solid lines) and state value function (shades of grey). The direction chosen by the agent is parallel to the streamlines. The target is represented with the red disk.

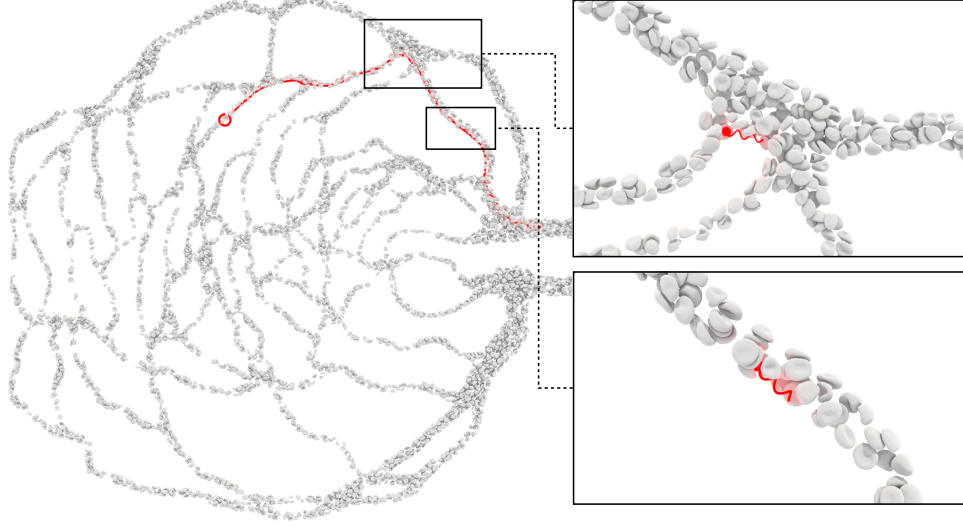


Figure 7: Trajectory of the ABF in the blood simulations with feedback control via the RL policy. The ABF reaches the target (red circle) and follows a trajectory (red line) similar to that obtained with the reduced order model. The zoomed-in views show the ABF swimming in the capillaries.

favor regions where the background velocity is the largest and aligned with the swimming direction, thus decreasing the overall travel time of the swimmer. When the swimmer is away from this line, the agent chooses a direction that brings the swimmer back to the line. This mechanism explains the robustness of the control policy to external perturbations.

Figure 6 shows the streamlines of the policy, together with the state-value function estimated during learning. The state-value function takes low values in regions where the swimmer cannot recover due to strong flow fields. Hence, in these regions, the policy is not meaningful. In regions away from the optimal path and with higher state-value function, the policy has a similar behavior to the policy along the optimal path: the streamlines converge near the centerline of the vessel, where the velocity is higher.

4 Control of the ABF in fine-grained blood simulations

The control policy trained on the reduced-order model is now tested in the fine-grained model. The policy maps the swimmer's position to the swimming direction \mathbf{p} . However, in the fine-grained simulations, the swimming direction is not set directly and we instead control the magnetic field. Given that ABFs align perpendicularly to the plane of the magnetic field's rotation, we adjust the magnetic field as

$$\mathbf{B}(t) = BR_x(\mathbf{p}) \begin{pmatrix} 0 \\ \cos \omega t \\ \sin \omega t \end{pmatrix}, \quad (7)$$

where B and ω are the magnitude and frequency of rotation of the magnetic field, respectively, and $R_x(\mathbf{p})$ is the rotation that transforms the vector \mathbf{e}_x into the swimming direction \mathbf{p} with axis of rotation $\mathbf{e}_x \times \mathbf{p}$. The direction \mathbf{p} is computed from the policy evaluated at the ABF's center of mass, and the magnetic field is adapted at every time step of the simulation.

Figure 7 (Multimedia available online) shows that the ABF successfully reaches the target using the policy that was previously learned from the reduced-order model. The ABF follows a trajectory similar to that observed in the reduced-order model. Additionally, the ABF tends to align with the flow direction

and the centerline of the capillaries, suggesting that the trajectory minimizes the travel time. Away from bifurcations, the policy seems to keep the ABF near the center of the capillaries, where the flow is faster. We observe that the ABF remains close to the wall boundaries in the vicinity of bifurcations. This strategy offers two benefits: the ABF is closer to the correct downstream branch, reducing the risk of taking the wrong bifurcation, and the ABF has a larger swimming speed relative to the flow, allowing finer control in these critical areas.

We emphasize that the policy was trained on an environment that is different from the fine-grained simulations but has a similar qualitative response. In the reduced-order model, we assume that the swimmer immediately reorients to the control output, which is not the case in the fine-grained blood model. Furthermore, the velocity field is different from that obtained from the Stokes solver with Newtonian assumption. Finally, the swimming speed of the ABF with respect to the fluid depends on the local hematocrit, the configuration of the surrounding RBCs, and the geometry of the capillaries, which we ignore in the reduced order model. A comparison of the ABF’s coordinates against time between the DPD simulations and the reduced order model is shown in the Supplementary Material. In both cases the ABF follows the same trajectory and has a similar travel time. We observe small differences in the swimming velocity, that may be due to the surrounding geometry, wall effects, and local hematocrit. Despite these differences, the policy learned by the RL agent in the reduced-order model is successful in the fine-grained simulations. This transfer indicates that RL is an effective method to learn policies that are robust to changes in the environment.

5 Outlook

In this study, we assume that the position of the ABF can be estimated in real time. However, in practice, the localization of micrometer-sized objects *in vivo* remains a significant challenge. Promising techniques, such as magnetic particle imaging (MPI) [50], ultrasound imaging [51] and fluorescence imaging [52], have shown potential for tracking magnetic microswimmers in biological environments, but further advances in spatial resolution are necessary to enable their practical application [53].

Furthermore, in this work, we have considered a single ABF, while it would be beneficial to control multiple ABFs to achieve targeted drug delivery or microsurgery. Controlling multiple ABFs of different shapes with a uniform magnetic field has been explored in the absence of wall boundaries [23], but this approach is currently limited to a few ABFs. An other potential approach to control a swarm of ABFs consists in exploiting the collective behavior of micro-objects through their magnetic interactions [54], although current research considers ideal setups of microrollers close to flat surfaces and no background flows.

6 Summary

We have performed simulations of the evolution of ABFs in the bloodstream through complex capillaries. The simulations employ a fine-grained blood model coupled with the DPD method to resolve the flow mechanics. The ABF is propelled via an external magnetic field, controlled by a RL agent with the aim of guiding the ABF towards a prescribed target. The agent was trained on a reduced order model that was calibrated from fine-grained blood simulations. This approach is much less computationally demanding than the use of blood simulations in the training phase. The control policy is robust to external noise in the reduced-order environment and is successful nearly 100% of the time for relatively large perturbations. Interestingly, the same control policy is also successful in fine-grained blood simulations.

These results demonstrate that control policies trained on reduced-order models are potent candidates for control in fine-grained simulations and possibly in real conditions, while requiring moderate computational resources. Furthermore, this approach enables the design of personalized control strategies based on patient-specific data, as we have shown in this case by using the reconstruction of capillary networks generated from fundus images. This method can be generalized to the navigation of microswimmers for targeted drug delivery and microsurgery at precise locations, potentially becoming a critical tool for personalized medicine.

Supplementary Material

The Supplementary Material provides details about the generation of the geometry file, a description about the calibration of the reduced-order model from DPD simulations, the parameters of the reinforcement learning algorithm, a comparison between the models, and analysis of the motion of the ABF in the DPD simulations.

Acknowledgments

We acknowledge the computational resources granted by the Swiss National Supercomputing Center (CSCS) under the project ID “s1160”.

Conflicts of Interest

The authors have no conflicts to disclose.

References

- [1] Fernando Soto, Jie Wang, Rajib Ahmed, and Utkan Demirci. Medical micro/nanorobots in precision medicine. *Advanced science*, 7(21):2002203, 2020.
- [2] Mandana T Manzari, Yosi Shamay, Hiroto Kiguchi, Neal Rosen, Maurizio Scaltriti, and Daniel A Heller. Targeted drug delivery strategies for precision medicines. *Nature Reviews Materials*, 6(4):351–370, 2021.
- [3] Ada-Ioana Bunea and Rafael Taboryski. Recent advances in microswimmers for biomedical applications. *Micromachines*, 11(12):1048, 2020.
- [4] Rémi Dreyfus, Jean Baudry, Marcus L Roper, Marc Fermigier, Howard A Stone, and Jérôme Bibette. Microscopic artificial swimmers. *Nature*, 437(7060):862–865, 2005.
- [5] Jiangfan Yu, Dongdong Jin, Kai-Fung Chan, Qianqian Wang, Ke Yuan, and Li Zhang. Active generation and magnetic actuation of microrobotic swarms in bio-fluids. *Nature communications*, 10(1):5631, 2019.
- [6] Mariana Medina-Sánchez, Lukas Schwarz, Anne K Meyer, Franziska Hebenstreit, and Oliver G Schmidt. Cellular cargo delivery: Toward assisted fertilization by sperm-carrying micromotors. *Nano letters*, 16(1):555–561, 2016.
- [7] Simone Schuerle, Ava P Soleimany, Tiffany Yeh, GM Anand, M Häberli, HE Fleming, Nima Mirkhani, Famin Qiu, Sabine Hauert, X Wang, et al. Synthetic and living micropropellers for convection-enhanced nanoparticle transport. *Science advances*, 5(4):eaav4803, 2019.
- [8] Xu Wang, Jun Cai, Lili Sun, Shuo Zhang, De Gong, Xinghao Li, Shuhua Yue, Lin Feng, and Deyuan Zhang. Facile fabrication of magnetic microrobots based on spirulina templates for targeted delivery and synergistic chemo-photothermal therapy. *ACS applied materials & interfaces*, 11(5):4745–4756, 2019.
- [9] Li Zhang, Jake J Abbott, Lixin Dong, Bradley E Kratochvil, Dominik Bell, and Bradley J Nelson. Artificial bacterial flagella: Fabrication and magnetic control. *Applied Physics Letters*, 94(6), 2009.
- [10] Li Zhang, Jake J Abbott, Lixin Dong, Kathrin E Peyer, Bradley E Kratochvil, Haixin Zhang, Christos Bergeles, and Bradley J Nelson. Characterizing the swimming properties of artificial bacterial flagella. *Nano letters*, 9(10):3663–3667, 2009.
- [11] Malay Pal, Itzhak Fouxon, Alexander M Leshansky, and Ambarish Ghosh. Fluid flow induced by helical microswimmers in bulk and near walls. *Physical review research*, 4(3):033069, 2022.

- [12] Ranabir Dey, Carola M Bunes, Babak Vajdi Hokmabad, Chenyu Jin, and Corinna C Maass. Oscillatory rheotaxis of artificial swimmers in microchannels. *Nature communications*, 13(1):2952, 2022.
- [13] Pooyath Lekshmy Venugopalan, Ranajit Sai, Yashoda Chandorkar, Bikramjit Basu, Srinivasrao Shivashankar, and Ambarish Ghosh. Conformal cytocompatible ferrite coatings facilitate the realization of a nanovoyager in human blood. *Nano letters*, 14(4):1968–1975, 2014.
- [14] Yunus Alapan, Ugur Bozuyuk, Pelin Erkoc, Alp Can Karacakol, and Metin Sitti. Multifunctional surface microrollers for targeted cargo delivery in physiological blood flow. *Science robotics*, 5(42):eaba5726, 2020.
- [15] Xiaojing Qi, Shuo Wang, Shuhao Ma, Keqin Han, Xin Bian, and Xuejin Li. Quantitative prediction of rolling dynamics of leukocyte-inspired microroller in blood flow. *Physics of Fluids*, 33(12), 2021.
- [16] Santiago Muiños-Landin, Alexander Fischer, Viktor Holubec, and Frank Cichos. Reinforcement learning with artificial microswimmers. *Science Robotics*, 6(52):eabd9285, 2021.
- [17] Chaojie Mo, Gaojin Li, and Xin Bian. Challenges and attempts to make intelligent microswimmers. *Frontiers in Physics*, 11:1279883, 2023.
- [18] Simona Colabrese, Kristian Gustavsson, Antonio Celani, and Luca Biferale. Flow navigation by smart microswimmers via reinforcement learning. *Physical review letters*, 118(15):158004, 2017.
- [19] Simona Colabrese, Kristian Gustavsson, Antonio Celani, and Luca Biferale. Smart inertial particles. *Physical Review Fluids*, 3(8):084301, 2018.
- [20] Luca Biferale, Fabio Bonaccorso, Michele Buzzicotti, Patricio Clark Di Leoni, and Kristian Gustavsson. Zermelo’s problem: optimal point-to-point navigation in 2D turbulent flows using reinforcement learning. *Chaos: An Interdisciplinary Journal of Nonlinear Science*, 29(10), 2019.
- [21] Jaya Kumar Alageshan, Akhilesh Kumar Verma, Jérémie Bec, and Rahul Pandit. Machine learning strategies for path-planning microswimmers in turbulent flows. *Physical Review E*, 101(4):043110, 2020.
- [22] Francesco Borra, Luca Biferale, Massimo Cencini, and Antonio Celani. Reinforcement learning for pursuit and evasion of microswimmers at low reynolds number. *Physical Review Fluids*, 7(2):023103, 2022.
- [23] Lucas Amoudruz and Petros Koumoutsakos. Independent control and path planning of microswimmers with a uniform magnetic field. *Advanced Intelligent Systems*, 4(3):2100183, 2022.
- [24] Petr Karnakov, Lucas Amoudruz, and Petros Koumoutsakos. Optimal navigation in microfluidics via the optimization of a discrete loss. *Physical Review Letters*, 134(4):044001, 2025.
- [25] Yangzhe Liu, Zhao Wang, and Alan CH Tsang. Reinforcement learning selects multimodal locomotion strategies for bioinspired microswimmers. *Soft Matter*, 21(12):2363–2373, 2025.
- [26] Yuguang Yang, Michael A Bevan, and Bo Li. Hierarchical planning with deep reinforcement learning for 3d navigation of microrobots in blood vessels. *Advanced Intelligent Systems*, 4(11):2200168, 2022.
- [27] Lucas Amoudruz, Athena Economides, and Petros Koumoutsakos. The volume of healthy red blood cells is optimal for advective oxygen transport in arterioles. *Biophysical Journal*, 123(10):1289–1296, 2024.
- [28] Pejman Ghassemi, Jianting Wang, Anthony J Melchiorri, Jessica C Ramella-Roman, Scott A Mathews, James C Coburn, Brian S Sorg, Yu Chen, and T Joshua Pfefer. Rapid prototyping of biomimetic vascular phantoms for hyperspectral reflectance imaging. *Journal of biomedical optics*, 20(12):121312–121312, 2015.

- [29] Lucas Amoudruz, Athena Economides, Georgios Arampatzis, and Petros Koumoutsakos. The stress-free state of human erythrocytes: Data-driven inference of a transferable RBC model. *Biophysical Journal*, mar 2023.
- [30] Robert D Groot and Patrick B Warren. Dissipative particle dynamics: Bridging the gap between atomistic and mesoscopic simulation. *The Journal of chemical physics*, 107(11):4423–4435, 1997.
- [31] Guido Novati and Petros Koumoutsakos. Remember and forget for experience replay. In *Proceedings of the 36th International Conference on Machine Learning*, 2019.
- [32] Alonso Marco, Felix Berkenkamp, Philipp Hennig, Angela P Schoellig, Andreas Krause, Stefan Schaal, and Sebastian Trimpe. Virtual vs. real: Trading off simulations and physical experiments in reinforcement learning with bayesian optimization. In *2017 IEEE International Conference on Robotics and Automation (ICRA)*, pages 1557–1563. IEEE, 2017.
- [33] Xue Bin Peng, Marcin Andrychowicz, Wojciech Zaremba, and Pieter Abbeel. Sim-to-real transfer of robotic control with dynamics randomization. In *2018 IEEE international conference on robotics and automation (ICRA)*, pages 3803–3810. IEEE, 2018.
- [34] Anil K Dasanna, Johannes Mauer, Gerhard Gompper, and Dmitry A Fedosov. Importance of viscosity contrast for the motion of erythrocytes in microcapillaries. *Frontiers in Physics*, 9:666913, 2021.
- [35] Frank Jülicher. The morphology of vesicles of higher topological genus: conformal degeneracy and conformal modes. *Journal de physique ii*, 6(12):1797–1824, 1996.
- [36] Gerald Lim H. W., Michael Wortis, and Ranjan Mukhopadhyay. Red Blood Cell Shapes and Shape Transformations: Newtonian Mechanics of a Composite Membrane. *Soft Matter*, 4, 2008.
- [37] Dmitry A Fedosov. *Multiscale modeling of blood flow and soft matter*. PhD thesis, Citeseer, 2010.
- [38] Lucas Amoudruz. *Simulations and Control of Artificial Microswimmers in Blood*. PhD thesis, ETH Zurich, 2022.
- [39] Alireza Yazdani, Mingge Deng, Bruce Caswell, and George Em Karniadakis. Flow in complex domains simulated by dissipative particle dynamics driven by geometry-specific body-forces. *Journal of Computational Physics*, 305:906–920, 2016.
- [40] Petr Karnakov, Fabian Wermelinger, Sergey Litvinov, and Petros Koumoutsakos. Aphros: High performance software for multiphase flows with large scale bubble and drop clusters. In *Proceedings of the Platform for Advanced Scientific Computing Conference*, pages 1–10, 2020.
- [41] Dmitry Alexeev, Lucas Amoudruz, Sergey Litvinov, and Petros Koumoutsakos. Mirheo: High-performance mesoscale simulations for microfluidics. *Computer Physics Communications*, 254:107298, 2020.
- [42] Rami Mhanna, Famin Qiu, Li Zhang, Yun Ding, Kaori Sugihara, Marcy Zenobi-Wong, and Bradley J Nelson. Artificial bacterial flagella for remote-controlled targeted single-cell drug delivery. *Small*, 10(10):1953–1957, 2014.
- [43] Debora Schamel, Marcel Pfeifer, John G Gibbs, Björn Miksch, Andrew G Mark, and Peer Fischer. Chiral colloidal molecules and observation of the propeller effect. *Journal of the American Chemical Society*, 135(33):12353–12359, 2013.
- [44] Peter J Vach, Nicolas Brun, Mathieu Bennet, Luca Bertinetti, Marc Widdrat, Jens Baumgartner, Stefan Klumpp, Peter Fratzl, and Damien Faivre. Selecting for function: solution synthesis of magnetic nanopropellers. *Nano letters*, 13(11):5373–5378, 2013.

- [45] Andrew Y Ng, Daishi Harada, and Stuart Russell. Policy invariance under reward transformations: Theory and application to reward shaping. In *ICML*, volume 99, pages 278–287. Citeseer, 1999.
- [46] Guido Novati, Lakshminarayanan Mahadevan, and Petros Koumoutsakos. Controlled gliding and perching through deep-reinforcement-learning. *Physical Review Fluids*, 4(9):093902, 2019.
- [47] Siddhartha Verma, Guido Novati, and Petros Koumoutsakos. Efficient collective swimming by harnessing vortices through deep reinforcement learning. *P. Natl. Acad. Sci.*, page 201800923, may 2018.
- [48] Ioannis Mandralis, Pascal Weber, Guido Novati, and Petros Koumoutsakos. Learning swimming escape patterns for larval fish under energy constraints. *Physical Review Fluids*, 6(9):093101, 2021.
- [49] Sergio M Martin, Daniel Wälchli, Georgios Arampatzis, Athena E Economides, Petr Karnakov, and Petros Koumoutsakos. Korali: Efficient and scalable software framework for bayesian uncertainty quantification and stochastic optimization. *Computer Methods in Applied Mechanics and Engineering*, 389:114264, 2022.
- [50] Anna C Bakenecker, Anselm von Gladiss, Thomas Friedrich, Ulrich Heinen, Heinrich Lehr, Kerstin Lüdtke-Buzug, and Thorsten M Buzug. Actuation and visualization of a magnetically coated swimmer with magnetic particle imaging. *Journal of Magnetism and Magnetic Materials*, 473:495–500, 2019.
- [51] Islam SM Khalil, Pedro Ferreira, Ricardo Eleutério, Chris L de Korte, and Sarthak Misra. Magnetic-based closed-loop control of paramagnetic microparticles using ultrasound feedback. In *2014 IEEE International Conference on Robotics and Automation (ICRA)*, pages 3807–3812. IEEE, 2014.
- [52] Qinglong Wang, Qianqian Wang, Zhipeng Ning, Kai Fung Chan, Jialin Jiang, Yuqiong Wang, Lin Su, Shuai Jiang, Ben Wang, Bonaventure Yiu Ming Ip, et al. Tracking and navigation of a microswarm under laser speckle contrast imaging for targeted delivery. *Science Robotics*, 9(87):eadh1978, 2024.
- [53] Salvador Pané, Josep Puigmartí-Luis, Christos Bergeles, Xiang-Zhong Chen, Eva Pellicer, Jordi Sort, Vanda Počepcová, Antoine Ferreira, and Bradley J Nelson. Imaging technologies for biomedical micro- and nanoswimmers. *Advanced Materials Technologies*, 4(4):1800575, 2019.
- [54] Gašper Kokot and Alexey Snezhko. Manipulation of emergent vortices in swarms of magnetic rollers. *Nature communications*, 9(1):2344, 2018.

Supplementary Material

Optimal navigation of magnetic artificial microswimmers in blood capillaries with deep reinforcement learning

Lucas Amoudruz¹, Sergey Litvinov¹, and Petros Koumoutsakos^{1,*}

¹School of Engineering and Applied Sciences, Harvard University, Cambridge, MA 02138, United States.

*corresponding author: petros@seas.harvard.edu

1 Generation of the geometry

The geometric representation of the capillaries is generated from an explicit representation (triangle mesh) obtained from ref. [1]. The triangle mesh was smoothed with a Laplacian filter and simplified to keep 10% of the faces in *Meshlab* [2]. This explicit representation of the surface is not convenient to check whether a particle is inside or outside the boundaries, and we thus employ an implicit representation stored on a uniform grid, the signed distance function (SDF). The SDF of the capillaries was generated from the triangle mesh on a domain of size $576 \times 528 \times 24$ (simulation units). The SDF takes into account the periodic images of the geometry, to ensure continuity across the periodic domain, a necessary feature to perform the dissipative particle dynamics (DPD) simulations. Furthermore, the SDF was merged with that of two cylinders that form the inlet and outlet of the geometry and are periodically connected (fig. 1). This periodic connection makes the domain fully periodic and simplifies particle simulations as no mechanism of inserting and deleting particles is needed.

The SDF geometric representation is usable by both *Aphros* [3] and *Mirheo* [4] to perform the Stokes and the detailed blood simulations, respectively. Furthermore it simplifies the implementation of the bounce-back of the swimmer in the simplified model, as a evaluating the SDF at the swimmer's position indicates if it is inside or outside of the capillaries. In the latter case, the swimmer is simply put to its previous position.

Figure 2 shows a two-dimensional slice of the velocity field obtained from *Aphros*. This field corresponds to an inlet of unit velocity and no-slip along the walls of the capillaries, and we assumed an incompressible, Newtonian fluid. This velocity field is used by the simplified model described in the main text.

2 ODE model to produce line in Fig. 2 of the manuscript

By linearity of the Stokes equation, the linear and angular velocities of a rigid object are linearly dependent on the external forces and torques applied to it [5]:

$$\begin{bmatrix} \mathbf{V} \\ \boldsymbol{\Omega} \end{bmatrix} = \begin{bmatrix} M^{FV} & M^{TV} \\ M^{F\Omega} & M^{T\Omega} \end{bmatrix} \begin{bmatrix} \mathbf{F} \\ \mathbf{T} \end{bmatrix}, \quad (1)$$

where the matrix coefficients are fixed in the frame of the object. In this study there is no external force and only the external magnetic torque,

$$\mathbf{T} = \mathbf{m} \times \mathbf{B},$$

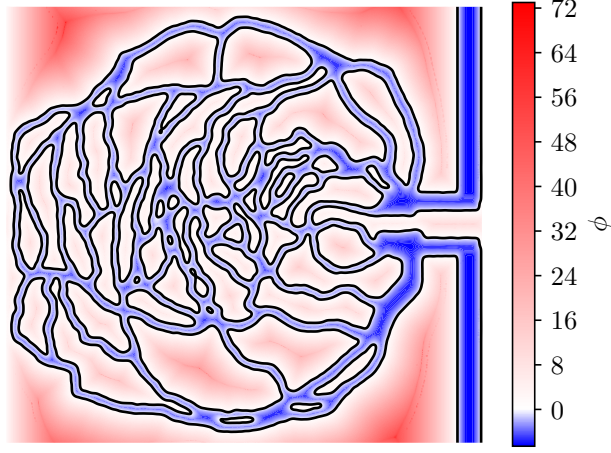


Figure 1: Slice $z = 12$ of the SDF $\phi(\mathbf{x})$ of the capillaries (grey scale) and corresponding zero-isoline (solid line). The SDF is negative inside the capillaries and positive outside. This implicit representation provides a convenient way to check whether a position is inside or outside the capillaries.

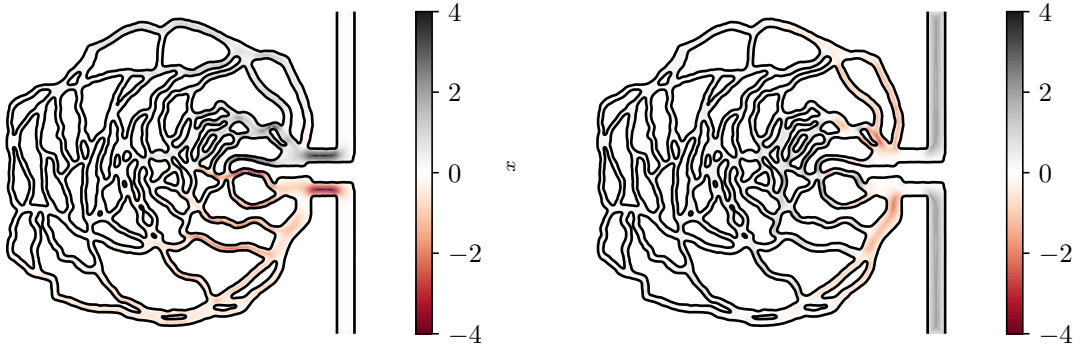


Figure 2: Slice of the velocity inside the capillaries obtained from the Stokes solver *Aphros*. The left and right plots correspond to the x and y components, respectively, and the solid line denotes the boundaries of the walls.

where \mathbf{m} is the magnetic moment of the artificial bacterial flagellum (ABF) (fixed in the frame of the swimmer) and \mathbf{B} is the external magnetic field. Considering an ABF swimming in the x direction, subjected to a rotating magnetic field in the yz plane,

$$\mathbf{B}(t) = \begin{bmatrix} 0 \\ B \cos \omega t \\ B \sin \omega t \end{bmatrix}, \quad (2)$$

where ω is the angular frequency of rotation of the magnetic field and B its magnitude. We assume that the swimmer rotates around the x axis. Defining θ as the angle between the y axis and the magnetic moment of the swimmer, we get $\dot{\theta} = \Omega$. The magnetic torque magnitude is given by $T_m = mB \sin(\omega t - \theta)$. Using eq. (1), the angular velocity of the swimmer is given by $\Omega = M_{11}^{T\Omega} T_m$, hence we get the following ODE:

$$\dot{\theta} = \omega_c \sin(\omega t - \theta), \quad (3)$$

where we have defined the critical angular frequency $\omega_c = M_{11}^{T\Omega} mB$.

When $\omega \leq \omega_c$, eq. (3) admits the steady solution $\theta(t) = \omega t + \phi$, where ϕ is a phase depending on the mobility matrix coefficients and the maximal magnetic torque amplitude. In this regime, the swimmer is able to rotate at the same frequency as that of the magnetic field rotation, since the magnetic torque is large enough to compensate for the hydrodynamic torque.

On the contrary, when $\omega > \omega_c$, the magnetic torque is too small to sustain the hydrodynamic torque that would be required to keep the swimmer rotating at the same angular frequency. The solution to eq. (3) has been solved in refs. [6, 7] and reads

$$\theta(t) = \omega t + 2 \arctan \left(\frac{-\omega_c + \sqrt{\omega_c^2 - \omega^2} \tan \left(-\frac{1}{2} \sqrt{\omega_c^2 - \omega^2} (t + \phi) \right)}{\omega} \right),$$

where ϕ depends on the initial conditions. The second term in the solution is periodic in time with angular frequency $\sqrt{\omega_c^2 - \omega^2}$. The effective (or time averaged) angular frequency of the swimmer is thus given by $\Omega = \omega - \sqrt{\omega_c^2 - \omega^2}$.

Using the mobility matrix relation, the linear velocity along x is linear with the angular velocity. Hence, we obtain that the velocity of the ABF changes with the magnetic frequency of rotation as

$$V(\omega) = \begin{cases} a\omega, & \text{if } \omega \leq \omega_c, \\ a \left(\omega - \sqrt{\omega_c^2 - \omega^2} \right), & \text{otherwise.} \end{cases} \quad (4)$$

The constant a depends on the geometry of the swimmer, while the step out frequency depends on both the geometry and the maximum magnetic torque applied on the swimmer.

3 Calibration of the simplified model

We consider an ABF of radius $r = 2 \mu\text{m}$ and length $l = 18.37 \mu\text{m}$ in a magnetic field that rotates with a frequency $f = 1 \text{ kHz}$. We define the angular frequency $\omega = 2\pi f$. The swimming speed of the ABF in blood is measured from 15 simulations with different initial cells configurations. The simulations consist of a single ABF swimming in a periodic tube of radius $R = 10 \mu\text{m}$. The tube is filled with a suspension of blood cells at $\text{Ht} = 25\%$ and the ABF is initially placed at the center of the tube. Figure 3 shows the displacement of the ABF over time for 15 trials of the simulation, and the mean squared deviation from the mean displacement of these trials. We estimate U as the slope of the mean displacement over time, and the diffusion coefficient D as the slope of $\langle \Delta x^2 \rangle$ against $6t$, where $\Delta x(t) = x(t) - Ut$. We find a swimming speed of $U = 8.40 \times 10^{-3} l \omega \approx 1 \text{ mm s}^{-1}$ and a diffusion coefficient (due to collisions with the surrounding cells) of $D_{\text{sim}} = 2.56 \times 10^{-4} l^2 \omega \approx 542 \mu\text{m}^2/\text{s}$.

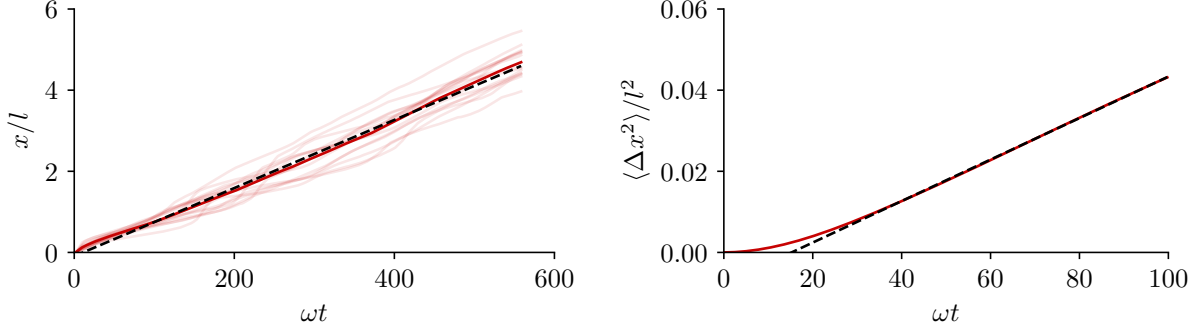


Figure 3: Left: Displacement x of the ABF for 15 simulations (shaded lines) against time. The solid line corresponds to the average displacement and the dashed line is a linear fit to this line. Right: Mean squared deviation from the mean displacement of the ABFs over 15 simulations against time (solid line) and linear fit of the non ballistic part (dashed line).

In the reduced order model, this corresponds to $U \approx U_{in} = 1$, where U_{in} is the average velocity at the inlet and $D_{sim} \approx 0.0123$ in simulation units. The noise is anisotropic and to account for the differences we use a larger value during training $D = 0.1 \approx 8.14D_{sim}$. Furthermore, we set $U = 0.2U_{in}$ in the simplified model, making the task more difficult but potentially more robust to the ABF being stuck by the surrounding cells.

4 Initial positions of the swimmers during the training phase

During training, the initial position of the swimmer is sampled from a Gaussian distribution with a mean μ and a standard deviation $\sigma = 8.7$. If the sampled position is not inside the vessels or if its distance to μ is larger than 2σ , a new sample is proposed, until it meets all criteria. The mean μ is chosen as the entry of the capillary network with 20% probability. Otherwise, it is randomly chosen from a set of 20 positions with equal probability. These positions were obtained as follows: First, 400 brownian particles were initialized at the target position and evolved for a time T_{max} with a background velocity field $-\mathbf{u}$ and the same diffusion coefficient as the swimmer. Second, 20 points from these trajectories were sampled using the farthest point strategy [8]. These initial positions are shown in fig. 4.

5 Hyper-parameters in the reinforcement learning setup

Each episode is ended when either the ABF reaches the target within a distance $\delta = 5$ or the simulation time is larger than $T_{max} = 500$. Actions are computed from the state every $\Delta t = 0.1$. The agent was trained with a self propelling speed of $U = 0.2$ and a noise level of $D = 0.1$, and the maximal velocity at the inlet was set to 1. The discount factor was set to $\gamma = 1$ and we used $C = U_{in}$ in the reward equation.

We used the default settings in *Korali* [9]. The initial exploratory noise level was set to 0.1 along each action direction. We used the Adam optimizer with a learning rate of 1×10^{-4} and a mini-batch size of 128. The parameters of the policy were updated after every experience. The replay memory has a size of 131072. The REFER parameters [10] were set to $\beta = 0.3$, $C_{max} = 4$, $D = 0.1$, $A = 0$. The policy is represented by a neural network with 2 hidden layers of 64 units each, separated by a tanh activation function.

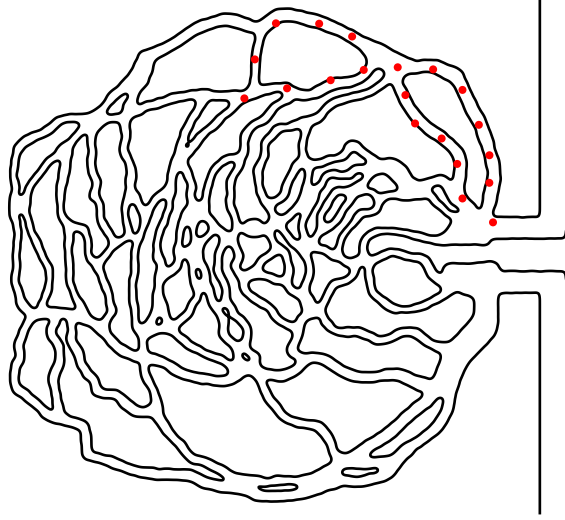


Figure 4: Position of the initial seeds to generate the initial positions of the swimmer at the beginning of each episode.

6 Comparison between the DPD model and the reduced order model

We compare the trajectories of the controlled ABF obtained from both the DPD simulations and the reduced order model. These trajectories are shown in fig. 5 and are similar with both models. The time taken to bring the swimmer to its target is similar in both cases.

7 Motion of the ABF in DPD simulations

Figure 6 shows the trajectory of the ABF in the DPD simulation around two bifurcations. As in the reduced order model, the trajectory tends to remain in the center of the vessels (see also fig. 7) and is tangent to the imposed swimming direction when the ABF is away from bifurcations.

However, when approaching a bifurcation, the control agent imposes a swimming direction towards the target branch, bringing the swimmer closer to the walls. Figure 7 shows that the speed of the ABF is lower at bifurcations than in vessels away from bifurcations. This is consistent with the controlled swimming direction not aligning with the velocity field of the background flow near bifurcations.

References

- [1] Pejman Ghassemi, Jianting Wang, Anthony J Melchiorri, Jessica C Ramella-Roman, Scott A Mathews, James C Coburn, Brian S Sorg, Yu Chen, and T Joshua Pfefer. Rapid prototyping of biomimetic vascular phantoms for hyperspectral reflectance imaging. *Journal of biomedical optics*, 20(12):121312–121312, 2015.
- [2] Paolo Cignoni, Marco Callieri, Massimiliano Corsini, Matteo Dellepiane, Fabio Ganovelli, Guido Ranzuglia, et al. Meshlab: an open-source mesh processing tool. In *Eurographics Italian chapter conference*, volume 2008, pages 129–136. Salerno, Italy, 2008.

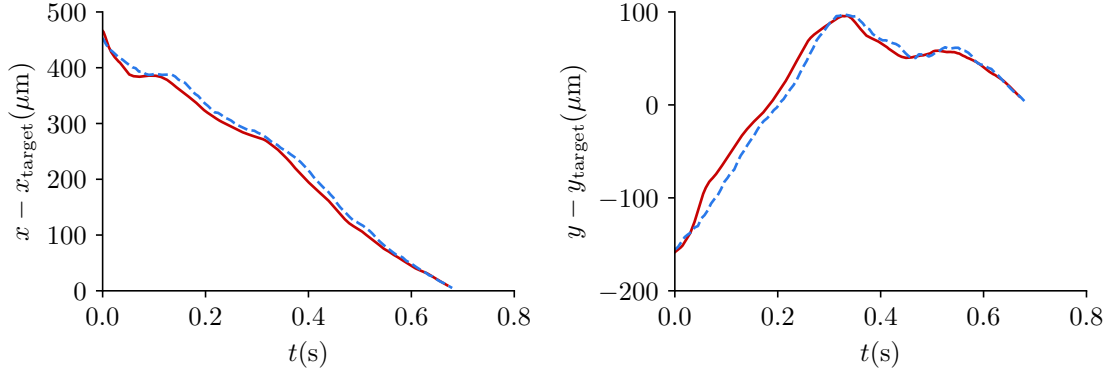


Figure 5: Comparison of the position of the swimmer with respect to its target from the DPD simulations (solid lines) and the reduced order model (dashed line) against time.

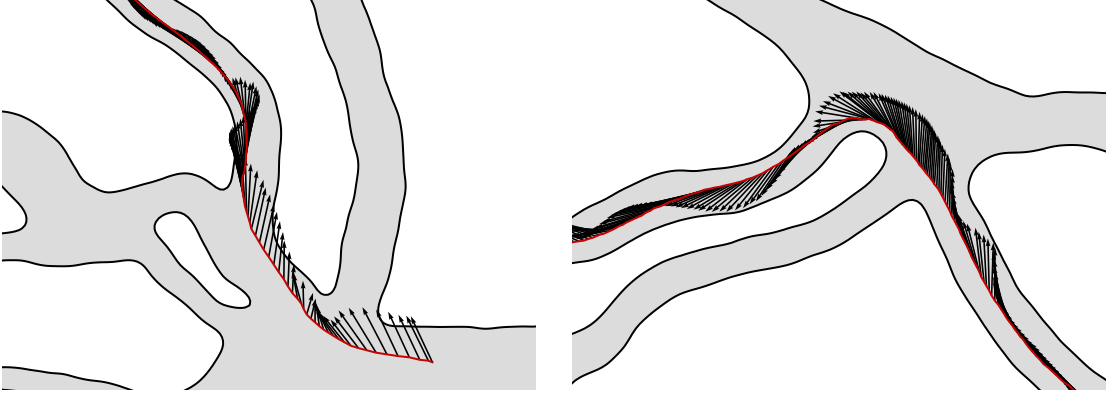


Figure 6: Trajectory of the ABF in the DPD simulation around two bifurcations (solid line) and swimming direction imposed by the policy (arrows).

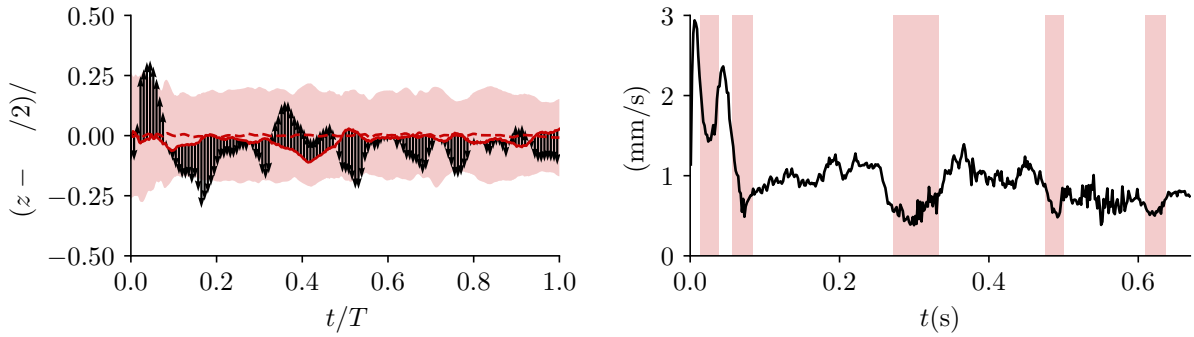


Figure 7: Left: z coordinate of the ABF against time in the DPD simulation (solid line) and z component of the swimming direction imposed by the policy (arrows). The shaded area indicates the wall positions in the vertical direction and the dashed line is the center of these lines. Right: Velocity of the ABF against time (solid line). Shaded regions indicate times when the ABF is at a bifurcation.

- [3] Petr Karnakov, Fabian Wermelinger, Sergey Litvinov, and Petros Koumoutsakos. Aphros: High performance software for multiphase flows with large scale bubble and drop clusters. In *Proceedings of the Platform for Advanced Scientific Computing Conference*, pages 1–10, 2020.
- [4] Dmitry Alexeev, Lucas Amoudruz, Sergey Litvinov, and Petros Koumoutsakos. Mirheo: High-performance mesoscale simulations for microfluidics. *Computer Physics Communications*, 254:107298, 2020.
- [5] Edward M Purcell. Life at low Reynolds number. *American journal of physics*, 45(1):3–11, 1977.
- [6] Debora Schamel, Marcel Pfeifer, John G Gibbs, Björn Miksch, Andrew G Mark, and Peer Fischer. Chiral colloidal molecules and observation of the propeller effect. *Journal of the American Chemical Society*, 135(33):12353–12359, 2013.
- [7] Peter J Vach, Nicolas Brun, Mathieu Bennet, Luca Bertinetti, Marc Widdrat, Jens Baumgartner, Stefan Klumpp, Peter Fratzl, and Damien Faivre. Selecting for function: solution synthesis of magnetic nanopropellers. *Nano letters*, 13(11):5373–5378, 2013.
- [8] Yuval Eldar, Michael Lindenbaum, Moshe Porat, and Yehoshua Y Zeevi. The farthest point strategy for progressive image sampling. *IEEE transactions on image processing*, 6(9):1305–1315, 1997.
- [9] Sergio M Martin, Daniel Wälchli, Georgios Arampatzis, Athena E Economides, Petr Karnakov, and Petros Koumoutsakos. Korali: Efficient and scalable software framework for bayesian uncertainty quantification and stochastic optimization. *Computer Methods in Applied Mechanics and Engineering*, 389:114264, 2022.
- [10] Guido Novati and Petros Koumoutsakos. Remember and forget for experience replay. In *Proceedings of the 36th International Conference on Machine Learning*, 2019.